

Soft Demodulator for Symbol-Level Precoding in Coded Multiuser MISO Systems

Yafei Wang, *Graduate Student Member, IEEE*, Hongwei Hou, *Graduate Student Member, IEEE*,
Wenjin Wang, *Member, IEEE*, Xiping Yi, *Member, IEEE*, Shi Jin, *Senior Member, IEEE*

Abstract—In this paper, we consider symbol-level precoding (SLP) in channel-coded multiuser multi-input single-output (MISO) systems. It is observed that the received SLP signals do not always follow Gaussian distribution, rendering the conventional soft demodulation with the Gaussian assumption unsuitable for the coded SLP systems. It, therefore, calls for novel soft demodulator designs for non-Gaussian distributed SLP signals with accurate log-likelihood ratio (LLR) calculation. To this end, we first investigate the non-Gaussian characteristics of both phase-shift keying (PSK) and quadrature amplitude modulation (QAM) received signals with existing SLP schemes and categorize the signals into two distinct types. The first type exhibits an approximate-Gaussian distribution with the outliers extending along the constructive interference region (CIR). In contrast, the second type follows some distribution that significantly deviates from the Gaussian distribution. To obtain accurate LLR, we propose the modified Gaussian soft demodulator and Gaussian mixture model (GMM) soft demodulators to deal with two types of signals respectively. Subsequently, to further reduce the computational complexity and pilot overhead, we put forward a novel neural soft demodulator, named pilot feature extraction network (PFEN), leveraging the transformer mechanism in deep learning. Simulation results show that the proposed soft demodulators dramatically improve the throughput of existing SLPs for both PSK and QAM transmission in coded systems.

Index Terms—Symbol-level-precoding, constructive interference region, non-Gaussian soft demodulator, transformer.

I. INTRODUCTION

IN multiuser multi-input multi-output (MU-MIMO) transmission, precoding is used to mitigate interference between users and increase spectral efficiency. Exploiting channel state information (CSI) at the transmitter/receiver, linear precoding schemes, such as the zero-forcing (ZF) precoding, have low computational complexity but cannot achieve the sum capacity in the finite signal-to-noise ratio (SNR) regime [1]–[4]. In contrast, symbol-level precoding (SLP), a nonlinear precoding method that leverages additional information from input data, goes beyond the performance achieved by linear precoding [5], [6]. Unlike the conventional precoding schemes that aim to suppress interference and noise, SLP schemes introduce constructive interference into the received signals. While conventional precoding schemes constrain the received signal to locate around the nominal constellations, SLP relaxes such constraint and allows the received signal to be distributed

within a pre-designed constructive interference region (CIR), leading to improved performance [5]–[21]. CIR is typically defined as the region more favorable to maximum-likelihood (ML) decision [16], based on which the two conventional optimizations, power minimization (PM) and signal-to-noise-plus-interference ratio (SINR) balancing, are redesigned for SLP transmission. The PM problem targets to minimize the total transmit power subject to SINR constraints [10]–[14], [16], [17], [22], and SINR balancing aims to maximize the minimum received SINR with limited transmit power [7], [11], [15], [17], [22]–[24]. Specifically, the problems with the CIR for phase-shift keying (PSK) and quadrature amplitude modulation (QAM) symbols are respectively investigated in [11] and [12], which are further formulated in various ways [7], [13]–[15], [17], [18]. Additionally, the concept of CIR has been expanded to generic constellations, enabling a more generalized definition beyond the conventional PSK and QAM symbols [16]. Apart from PM and SINR balancing, symbol error rate (SER) minimization is also a crucial problem in SLP transmission [19], [21], [25], [26], which generally further relaxes the constraint on the received signal distribution for lower SER. The SER minimization problem for PSK is considered in [19], while a deep-learning transceiver and an intelligent reflecting surface are introduced to minimize the SER for QAM in [26] and [21], respectively.

While attaining remarkable performance in uncoded systems, the freely distributed SLP signals impose significant challenges on soft demodulation for coded systems. Specifically, the received SLP signals are allowed to be freely distributed on the constellation map, exhibiting distinct non-Gaussian distributions for different SLP schemes [11], [19], [26], and therefore different log-likelihood ratio (LLR) calculations for soft demodulation. Since conventional soft demodulators calculate LLR based on the assumption of Gaussian distribution, the presence of non-Gaussian signals poses challenges in computing the LLR for the coded system [6], [27], [28]. However, to the best of our knowledge, little effort has been devoted to the investigation of soft demodulation for SLP with non-Gaussian received signals [6]. Although some studies have explored the LLR calculation of non-Gaussian received signals [29]–[31], these methods are limited to scenarios with specific noise distribution, which is inapplicable to the SLP signals in coded systems. The main reason is that the distribution of SLP signals is quite different from previous studies, and more noticeably varies across different channel settings, constellation mappings, and SLP schemes. The above analysis raises a critical question: *How to design effective and*

Manuscript received xxx.

Yafei Wang, Hongwei Hou, Wenjin Wang, Xiping Yi, and Shi Jin are with the National Mobile Communications Research Laboratory, Southeast University, Nanjing 210096, China (e-mail: wangyf@seu.edu.cn; hongwei-hou@seu.edu.cn; wangwj@seu.edu.cn; xyi@seu.edu.cn; jinshi@seu.edu.cn).

efficient soft demodulators for coded SLP transmission?

In this paper, we analyze the properties of the non-Gaussian received signal distribution and investigate new soft demodulators to obtain accurate LLR from the received signals. The major contributions of our work are summarized as follows:

- We first investigate the non-Gaussian characteristics of both PSK and QAM signals with existing SLP schemes and analyze their effect on LLR calculation. Based on the difference in received signal distributions, we categorize the non-Gaussian signals into two distinct types. The first type exhibits an approximate Gaussian distribution with the exception of a few probabilities extending along the CIR, and the second type has the distribution far deviated from the Gaussian distribution.
- We propose new soft demodulators for coded SLP systems with non-Gaussian received signals. Specifically, we propose a modified Gaussian soft demodulator for the first type of received signals. For the second type, we put forward a Gaussian mixture model (GMM) soft demodulator that approximates the non-Gaussian signal distribution by GMMs, with GMM parameters estimated from the received pilot signals. By exploiting the symmetry of the signal distributions corresponding to different constellation points, we propose a transform function, which reduce the number of unknown parameters and further decrease the pilot overhead. Simulation results demonstrate that GMM soft demodulators significantly improve the throughput of existing SLPs with PSK and QAM in coded systems.
- To avoid the iterative computation in GMM demodulator and the sharp performance decrease when pilot length is reduced, we propose the pilot feature extraction network (PFEN) soft demodulator, a deep-learning network trained to compute the optimal GMM parameters for received data signals from limited-length pilot signals. The PFEN employs transformer modules with permutation invariance to comprehensively extract the features from the inputs, i.e., the received pilot signals and rescaling factor. Compared with the GMM demodulator, the PFEN demodulator requires lower complexity and fewer pilot overheads while maintaining excellent performance.

This paper is structured as follows: In Section II, we introduce the system model and CIR. Section III analyzes the non-Gaussian distribution of the received signals. Section IV investigates modified Gaussian, GMM, and PFEN soft demodulators. Section V reports the simulation results, and the paper is concluded in Section VI.

Notation: $(\cdot)^{-1}$, $(\cdot)^T$, $(\cdot)^H$ denote the transpose and the transpose-conjugate operations, respectively. x , \mathbf{x} , and \mathbf{X} respectively denote a scalar, column vector, and matrix. $\Re(\cdot)$ and $\Im(\cdot)$ represent the real and imaginary part of a complex scalars, vector or matrix. $j = \sqrt{-1}$ denote imaginary unit. \in denotes belonging to a set, and \sim denote being distributed as. The expression $\mathcal{CN}(\mu, \sigma^2)$ represents circularly symmetric Gaussian distribution with mean μ and variance σ^2 . $\mathbb{R}^{M \times N}$ and $\mathbb{C}^{M \times N}$ respectively denote the sets of $M \times N$ real- and complex-valued matrices. $\mathcal{A} \setminus \mathcal{B}$ means objects that belong

to set \mathcal{A} and not to \mathcal{B} . ∇f denotes gradient of function $f(\cdot)$. $|\mathcal{A}|$ represents the cardinality of set \mathcal{A} . $\text{sign}(\cdot)$ denotes the sign function. $\angle(x)$ denotes the angle of complex scalar x . $\lfloor \cdot \rfloor$ represents the floor function. \mathbf{I}_K denotes $K \times K$ identity matrix. $\|\cdot\|_2$ denotes l_2 -norm. $\det(\mathbf{A})$ represents the determinant of matrix \mathbf{A} .

II. SYSTEM AND SIGNAL MODEL

A. System Model

Consider an MU-MISO downlink system where an N -antenna base station (BS) transmits the signal to K single-antenna user equipment (UE). We assume block flat fading channels where the channel coefficients remain constant for a coherence interval of L symbol durations. The channel between BS and the k -th UE is denoted as $\mathbf{h}_k \in \mathbb{C}^{N \times 1}$. The channel matrix $\mathbf{H} = [\mathbf{h}_1, \mathbf{h}_2, \dots, \mathbf{h}_K]^T$ is assumed to be available at the BS.

We consider the SLP system where the received signal of k -th UE at l -th symbol duration is

$$y_k[l] = \mathbf{h}_k^T \mathbf{x}[l] + n_k[l], \quad \forall k \in \mathcal{K}, \quad (1)$$

where $\mathcal{K} = \{1, 2, \dots, K\}$, $n_k[l] \sim \mathcal{CN}(0, \sigma^2)$ denotes the additive noise at the k -th UE and σ^2 represents the noise variance. $\mathbf{x}[l] \in \mathbb{C}^{N \times 1}$ is the transmit signal vector encoded by the symbol-level precoder for the transmission of $\mathbf{s}[l]$, which contains K independent QAM or PSK symbols

$$\mathbf{s}[l] = [s_1[l], s_2[l], \dots, s_K[l]]^T, \quad (2)$$

where $s_k[l]$ is the symbol desired by the k -th UE. These symbols are drawn from the constellation set $\mathcal{V} = \{v_q\}_{q \in \mathcal{Q}}$, where $\mathcal{Q} = \{1, \dots, Q\}$ and v_q represents q -th type of constellation point.

Due to the distinct SLP schemes to obtain $\mathbf{x}[l]$, the distribution of the received signal varies accordingly. We start with the mostly adopted SLP, i.e., CI-based SINR balancing (CISB) [7], [15], [18], and then extend the results to other schemes. The transmit signal can be written as [18], [22]

$$\mathbf{x}[l] = \gamma[l] \cdot \mathbf{H}^\dagger \tilde{\mathbf{s}}[l], \quad (3)$$

where $\gamma[l] = \sqrt{\frac{P_T[l]}{\|\mathbf{H}^\dagger \tilde{\mathbf{s}}[l]\|_2^2}}$, $\mathbf{H}^\dagger = \mathbf{H}^H (\mathbf{H}\mathbf{H}^H)^{-1}$, and $P_T[l]$ represents the transmit power. $\tilde{\mathbf{s}}[l] = [\tilde{s}_1[l], \tilde{s}_2[l], \dots, \tilde{s}_K[l]]^T$ denotes the target signal vector, where $\tilde{s}_k[l]$ is constrained in the CIR of $s_k[l]$ and optimized to maximize $\gamma[l]$ [15]. Substituting (3) into (1), we have

$$y_k[l] = \gamma[l] \tilde{s}_k[l] + n_k[l]. \quad (4)$$

The CIR $\mathcal{D}_k[l]$ is the modulation-specific region where the interference component of the received signal is CI [6], [7], [16]. Here CI refers to the interference that pushes the noise-free received signal away from the ML decision boundaries. As illustrated in Fig. 1, the CIR (green areas) allows CI to extend outer real and imaginary parts of the signal while maintaining the performance of inner ones [6]. It is worth noting that, for QAM, there are two types of constellation points, inner and outer (lateral and corner) ones, while the PSK only has outer (corner) ones.

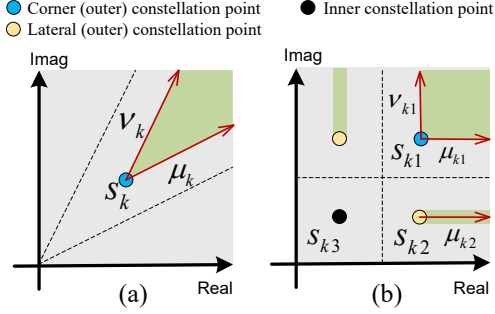


Fig. 1. CIRs and their boundary vectors of (a) PSK and (b) QAM.

B. Signal Model for Demodulation

When multi-level QAM is employed, the received signals are required to be scaled for correct demodulation [32], and the signal to be demodulated turns to $\bar{y}_k[l] = y_k[l]/\gamma[l] = \tilde{s}_k[l] + n_k[l]/\gamma[l]$. In practical block transmission, BS needs to broadcast $\gamma[l]$ to UEs at a symbol level, which results in excessive signaling overheads. One method to facilitate practical demodulation is that BS employs the power allocation scheme in [32] to unify $\gamma[l]$ in a transmission block:

$$\bar{\gamma} = \sqrt{\frac{\sum_{l=1}^L P_T[l]}{\sum_{l=1}^L \frac{P_T[l]}{\gamma^2[l]}}, \quad \bar{\mathbf{x}}[l] = \frac{\bar{\gamma}}{\gamma[l]} \mathbf{x}[l], \quad \forall l \in \mathcal{L}, \quad (5)$$

where $\mathcal{L} = \{1, 2, \dots, L\}$. Since PSK does not modulate the amplitude, rescaling and power allocation are optional. According to (4) and (5), the signal to be demodulated can be expressed as

$$\text{QAM} : \bar{y}_k[l] = \tilde{s}_k[l] + \frac{n_k[l]}{\bar{\gamma}}, \quad (6)$$

$$\text{PSK} : \bar{y}_k[l] = \begin{cases} \tilde{s}_k[l] + \frac{n_k[l]}{\bar{\gamma}}, & \text{WR} \\ \gamma[l]\tilde{s}_k[l] + n_k[l], & \text{WOR} \end{cases}, \quad (7)$$

where we use ‘WR’ and ‘WOR’ to represent ‘with rescaling’ and ‘without rescaling’ for convenience, respectively.

When the ML decision rule is applied in an uncoded system, the symbol in \mathcal{V} that is closest to the received signal in Euclidean distance is chosen for demodulation [33]. By maximizing $\gamma[l]$, SLP increases the received SNR and achieves a lower symbol error rate (SER) than conventional precoding schemes [11]. In addition, the CI in $\tilde{s}_k[l]$ pushes the signal away from the ML decision boundary and further reduces the SER. It is worth noting that these advantages brought by SLP are attainable for uncoded systems. When it comes to the coded systems with channel coding, however, it calls for new treatments for soft demodulation.

C. Soft Demodulation

Fig. 2 shows the multi-user coded systems with SLP, which includes channel encoders, channel (soft) decoders, and soft demodulators. Channel coding is an essential technique in practical communication systems, which usually employs an iterative soft decoder to approximate the optimal performance [34]. The LLR, as the output of the soft demodulator, is

the sole input to the iterative soft decoder, whose exactness determines the performance of the iterative soft decoder [35], [36].

For brevity of real representation, we define¹

$$\mathbf{v}_q = \begin{bmatrix} \Re(v_q) \\ \Im(v_q) \end{bmatrix}, \quad \mathbf{y}[l] = \begin{bmatrix} \Re(\bar{y}_k[l]) \\ \Im(\bar{y}_k[l]) \end{bmatrix}. \quad (8)$$

In general, symbols in \mathcal{V} are transmitted with equal probability, and the LLR can be acquired from below [37]

$$\text{LLR}_i[l] = \ln \frac{\sum_{\mathbf{v}_q \in \mathcal{S}_i^+} f_Y(\mathbf{y}[l]|\mathbf{v}_q)}{\sum_{\mathbf{v}_q \in \mathcal{S}_i^-} f_Y(\mathbf{y}[l]|\mathbf{v}_q)}, \quad (9)$$

where $\text{LLR}_i[l]$ denotes the LLR for i -th coded bit of $\mathbf{y}[l]$, and $f_Y(\mathbf{y}|\mathbf{v}_q)$ is the likelihood function [36]. \mathcal{S}_i^+ and \mathcal{S}_i^- are the sets of symbols whose i -th bit is 1 and 0, respectively.

III. THE EFFECT OF NON-GAUSSIAN RECEIVED SIGNALS ON DEMODULATION

The conventional Gaussian soft demodulator works under the assumption that $f_Y(\mathbf{y}|\mathbf{v}_q)$ is the probability density function (PDF) of a complex Gaussian distribution and can be expressed as [38]

$$f_Y(\mathbf{y}|\mathbf{v}_q) = \frac{\exp\left(-\frac{\|\mathbf{y}-\mathbf{v}_q\|_2^2}{\sigma_s^2}\right)}{\pi\sigma_s^2}, \quad \forall q \in \mathcal{Q}, \quad (10)$$

where σ_s^2 is the variance. However, the received signals of SLP schemes unlikely follow the Gaussian distribution, due to the presence of CI in the received signal. In particular, the received signals of SLP exhibit a departure from this assumption, i.e., $f_Y(\mathbf{y}|\mathbf{v}_q)$ with SLP is not Gaussian distributed.

In the scenario of $N = K = 8$, Rayleigh channel, and $\text{SNR} = P_T/\sigma^2 = 20\text{dB}$, Fig. 3 shows $f_Y(\mathbf{y}|\mathbf{v}_q)$ of three types of constellation points with CISB. We approximate $f_Y(\mathbf{y}|\mathbf{v}_q)$ using Monte Carlo simulations combined with statistical histograms, where the number of points within each square region is divided by their maximum value for normalization. In Fig. 3 (a), the distribution of $f_Y(\mathbf{y}|\mathbf{v}_q)$ exhibits a uniform circular pattern. In Fig. 3 (b), apart from the central circular pattern, $f_Y(\mathbf{y}|\mathbf{v}_q)$ further extends along both sides of the decision boundary. In Fig. 3 (c), the central distribution appears in a linear pattern, accompanied by extended portions. Evidently, $f_Y(\mathbf{y}|\mathbf{v}_q)$ does not adhere strictly to a Gaussian distribution.

A. Properties of Non-Gaussian Received Signals

In this subsection, we focus on the received signals of SLP and analyze the impact of their non-Gaussian distribution on the conventional soft demodulator.

According to (9), computing LLR requires the PDF $f_Y(\mathbf{y}|\mathbf{v}_q)$. As shown in (7), while $n_k[l] \sim \mathcal{CN}(0, \sigma^2)$ and $\bar{\gamma}$ can be seen as a constant when L is long enough, $f_Y(\mathbf{y}|\mathbf{v}_q)$

¹We focus on the demodulator of a single UE, so the index k is temporarily omitted in $\mathbf{y}[l]$.

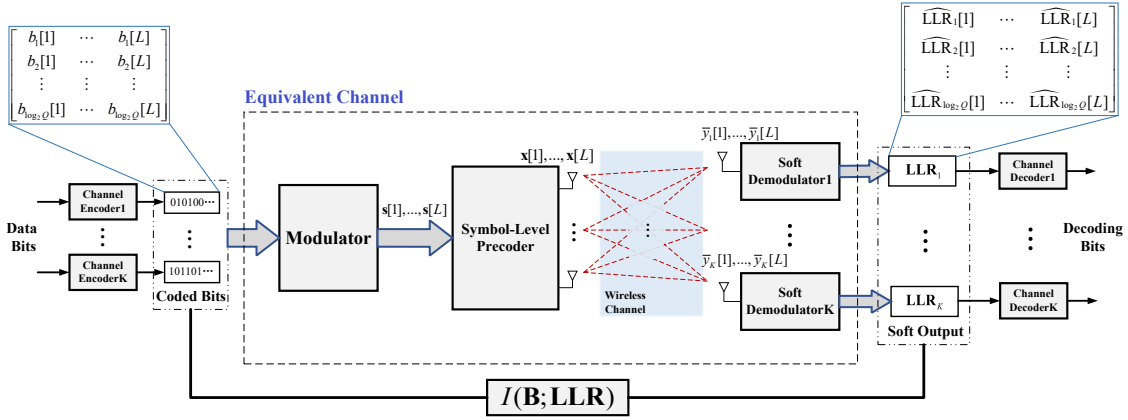


Fig. 2. Coded wireless communication system with SLP.

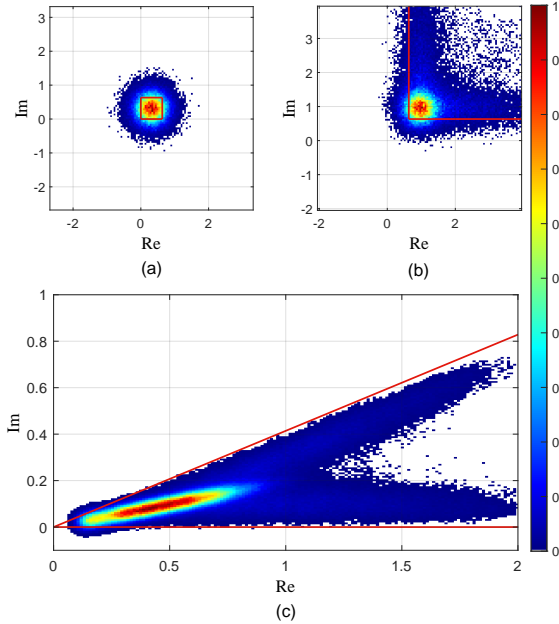


Fig. 3. Normalized $f_Y(\mathbf{y}|\mathbf{v}_q)$ with CISB where \mathbf{v}_q is (a) inner constellation point from 16QAM. (b) corner constellation point from 16QAM. (c) constellation point from 16PSK (WOR). The red lines represent the decision boundaries.

is determined by the distribution of $\tilde{s}_k[l]$ and $\gamma[l]\tilde{s}_k[l]$. $\tilde{\mathbf{s}}[l]$ can be obtained by solving the following problem [18], [39]:

$$\min_{\tilde{\mathbf{s}}} \|\mathbf{H}^\dagger \tilde{\mathbf{s}}\|_2^2 \quad \text{s.t.} \quad \tilde{s}_k \in \mathcal{D}_k[l], \forall k \in \mathcal{K}. \quad (11)$$

Since $\mathcal{D}_k[l]$ depends on $s_k[l]$, the above expression reveals that the change of $s_{k'}[l]$, $k' \in \mathcal{K} \setminus k$ affects the optimal $\tilde{s}_k[l]$ of a fixed $s_k[l]$. We define

$$\mathbf{s}_{\mathcal{K} \setminus k}[l] \triangleq [s_1[l] \quad \dots \quad s_{k-1}[l] \quad s_{k+1}[l] \quad \dots \quad s_K[l]]^T, \quad (12)$$

$$\mathcal{V}^K \triangleq \{\mathbf{s} : \mathbf{s} = [s_1 \quad s_2 \quad \dots \quad s_K]^T, \forall s_k \in \mathcal{V}\}, \quad (13)$$

where $\mathbf{s}_{\mathcal{K} \setminus k}[l]$ represents the vector composed of the parts of $\mathbf{s}[l]$ except for $s_k[l]$. We have $\mathbf{s}_{\mathcal{K} \setminus k}[l] \in \mathcal{V}^{K-1}$, and user symbols in $\mathbf{s}_{\mathcal{K} \setminus k}[l]$ has Q^{K-1} combinations, i.e., $|\mathcal{V}^{K-1}| = Q^{K-1}$. Based on the definition of $\mathbf{s}_{\mathcal{K} \setminus k}[l]$, we denote $\tilde{\mathbf{s}}_{\alpha|v_q}^*$

as the optimal solution of problem (11) with $s_k[l] = v_q$ and $\mathbf{s}_{\mathcal{K} \setminus k}[l] = \alpha$, where it can be concluded from the constraint in (11) that $[\tilde{\mathbf{s}}_{\alpha|v_q}^*]_k \in \mathcal{D}_k[l]$. According to the definition of $\gamma[l]$, we further define $\gamma_{\alpha|v_q} = \sqrt{P_T[l] / \|\mathbf{H}^\dagger \tilde{\mathbf{s}}_{\alpha|v_q}^*\|_2^2}$. Assume constellation points in \mathcal{V} are transmitted with equal probability. Therefore, we have

$$\begin{aligned} P(\tilde{s}_k[l] = [\tilde{\mathbf{s}}_{\alpha|v_q}^*]_k | s_k[l] = v_q) &= P(\gamma[l] = \gamma_{\alpha|v_q} | s_k[l] = v_q) \\ &= \frac{1}{Q^{K-1}}, \quad \alpha \in \mathcal{V}^{K-1}, \end{aligned} \quad (14)$$

based on which the distribution of $\tilde{s}_k[l]$ and $\gamma[l]\tilde{s}_k[l]$ can be obtained.

Considering that the solution of problem (11) is a non-intuitive process, we analyze $f_Y(\mathbf{y}|v_q)$ with the support of Fig. 3:

- **Inner QAM constellation point:** According to Fig. 1, when $s_k[l] = v_q$ and v_q is the inner constellation point, we have $\tilde{s}_k[l] = s_k[l]$, based on which $\bar{y}_k[l]$ with rescaling in (6), (7) is expressed as

$$\bar{y}_k[l] = s_k[l] + \overbrace{n_k[l]/\bar{\gamma}}^{\text{Gaussian random variable}}. \quad (15)$$

$\bar{y}_k[l]$ is a Gaussian random variable with mean v_q , and its distribution is shown in Fig. 3 (a).

- **Outer QAM/PSK constellation point (WR):** According to (6), (7) and (14), when $s_k[l] = v_q$ and v_q is the outer constellation point, $\bar{y}_k[l]$ with rescaling is expressed as

$$\bar{y}_k[l] = \underbrace{\tilde{s}_k[l]}_{\text{discrete random variable located in } \mathcal{D}_k[l]} + \overbrace{n_k[l]/\bar{\gamma}}^{\text{Gaussian random variable}}. \quad (16)$$

The random variable $\bar{y}_k[l]$ is the sum of a discrete random variable $\tilde{s}_k[l]$ located in $\mathcal{D}_k[l]$ and an independent Gaussian random variable $n_k[l]/\bar{\gamma}$. The posteriori distribution of $\tilde{s}_k[l]$ is given in (14), and $f_Y(\mathbf{y}[l]|v_q)$ is shown in Fig. 3. It is worth noting that since only some combinations of $\mathbf{s}_{\mathcal{K} \setminus k}[l]$ can exploit CI from $s_k[l]$ and there still exists $\tilde{s}_k[l] = s_k[l]$ in most cases, which means $f_Y(\mathbf{y}[l]|v_q)$ can

be approximated as the PDF of the Gaussian distribution followed by $v_q + n_k[l]/\bar{\gamma}$ like (15). However, due to the presence of $\tilde{s}_k[l]$ extending towards CIR, assuming $f_Y(\mathbf{y}[l]|\mathbf{v}_q)$ to be Gaussian distributed will introduce a mismatching error for parameter estimation, i.e.,

$$\begin{aligned}\hat{\sigma}_s^2 &= \mathbb{E} \{ (\bar{y}_k[l] - s_k[l])^2 \} \\ &= \mathbb{E} \{ (\tilde{s}_k[l] - s_k[l])^2 \} + \mathbb{E} \{ (n_k[l]/\bar{\gamma})^2 \} \\ &\geq \mathbb{E} \{ (n_k[l]/\bar{\gamma})^2 \},\end{aligned}\quad (17)$$

where $\hat{\sigma}_s^2$ is the parameters that the Gaussian soft demodulator is expected to estimate in (10), and $\mathbb{E} \{ (n_k[l]/\bar{\gamma})^2 \}$ is the variance of the Gaussian distribution followed by $v_q + n_k[l]/\bar{\gamma}$.

- **PSK constellation point (WOR):** According to (7) and (14), $\bar{y}_k[l]$ without rescaling is expressed as

$$\bar{y}_k[l] = \underbrace{\gamma[l]}_{\text{scalar random variable}} \cdot \underbrace{\tilde{s}_k[l]}_{\text{discrete random variable located in } \mathcal{D}_k[l]} + \underbrace{n_k[l]}_{\text{Gaussian random variable}}. \quad (18)$$

Different from (16), $\gamma[l]$ in (18) can adjust the radial scaling of $\tilde{s}_k[l]$, resulting in $\bar{y}_k[l]$ exhibiting a distribution that resembles stripes, which is shown in Fig. 3 (c).

In summary, $f_Y(\mathbf{y}|\mathbf{v}_q)$ with SLP usually does not follow Gaussian distribution. Thus, estimating the parameters of $f_Y(\mathbf{y}|\mathbf{v}_q)$ by treating it as Gaussian in the soft demodulator will lead to inaccurate LLRs, which will degrade the performance of the soft decoder.

Including the analyzed CISB, different SLP schemes result in different distributions of the received signals. In order to facilitate the subsequent design of soft demodulators, we classify the received signals from different modulation and SLP schemes into the following two types:

- **Type I:** This type of signal consists of QAM received signals with SLP schemes like CISB and CIMMSE [39]. The received signals of the inner QAM constellation points follow Gaussian distributions like Fig. 3 (a), while the received signals of the outer ones approximately exhibit a Gaussian distribution with the exception of few probabilities extending along the CIR like Fig. 3 (b). We propose the soft demodulator for this type of signals in Section IV-A.
- **Type II:** This type of signal consists of all PSK received signals (with and without rescaling). It also consists of QAM signals with SLP schemes whose signal distributions may deviate significantly from a Gaussian distribution [6], [19], [21], [26]. To provide an instance of such SLPs for the design and performance validation of the soft demodulator, we introduce the SLP for average SER minimization (ASM) in [40].² We propose soft demodulators for this type of signal in Sections IV-B and IV-C.

²Its signals exhibit a non-Gaussian distribution, and for the sake of readability, we illustrate the distribution in Figure 7 (a3) and (b3) in Section V.

IV. SOFT DEMODULATORS FOR NON-GAUSSIAN RECEIVED SIGNALS

A. Modified Gaussian Soft Demodulator

In this subsection, we design the modified Gaussian soft demodulator for SLP schemes whose received signals belong to **Type I**. The soft demodulator approximates the received signal distribution of the outer QAM constellation point in (16) as the Gaussian distribution with mean v_q . As the Gaussian distribution in (16) has the same variance as that in (15), the demodulator estimates the variance from the received signals belonging to inner QAM constellation points. It then applies the variance to $f_Y(\mathbf{y}[l]|\mathbf{v}_q)$ belonging to outer ones in (16), which prevents the problem of overestimating in (17).

We consider pilot-assisted transmission, where a transmission block contains some pilot signals whose transmit symbols are known to UE. The received signals $\mathbf{Y} \in \mathbb{R}^{L \times 2}$ in a transmission block at UE can be expressed as

$$\begin{aligned}\mathbf{Y} &= [\mathbf{y}[1] \quad \mathbf{y}[2] \quad \cdots \quad \mathbf{y}[L]]^T \\ &= [\mathbf{Y}_p^T \quad \mathbf{Y}_d^T]^T,\end{aligned}\quad (19)$$

where \mathbf{Y}_p and \mathbf{Y}_d are the received pilot signals and received data signals given by

$$\mathbf{Y}_p = [\mathbf{y}^p[1] \quad \mathbf{y}^p[2] \quad \cdots \quad \mathbf{y}^p[L_P]]^T \in \mathbb{R}^{L_P \times 2}, \quad (20)$$

$$\mathbf{Y}_d = [\mathbf{y}^d[1] \quad \mathbf{y}^d[2] \quad \cdots \quad \mathbf{y}^d[L_D]]^T \in \mathbb{R}^{L_D \times 2}, \quad (21)$$

where L_P is the number of pilot symbols, L_D is the number of data symbols, and $L_P + L_D = L$. According to the corresponding transmit symbols, the receiver can divide \mathbf{Y}_p into the following Q signal sets:

$$\mathcal{Y}_0, \mathcal{Y}_1, \dots, \mathcal{Y}_q, \dots, \mathcal{Y}_{Q-1}, \quad (22)$$

where $\mathcal{Y}_q = \{\mathbf{y}_q^p[1], \dots, \mathbf{y}_q^p[L_q]\}$ represents the set of received pilot signals whose transmit symbols are \mathbf{v}_q , and L_q is the number of signals in \mathcal{Y}_q which satisfies $\sum_{q=0}^{Q-1} L_q = L_P$. Note that signals in \mathcal{Y}_q are the samples from $f_Y(\mathbf{y}|\mathbf{v}_q)$.

For convenience in subsequent expressions, we define $\mathcal{Q} = \{0, 1, \dots, Q-1\}$ and denote the index sets of inner symbols, corner symbols, and lateral symbols as \mathcal{Q}_I , \mathcal{Q}_C , and \mathcal{Q}_L , respectively. Besides, we set the symbol indexes \mathcal{Q} in consecutive order on the constellation map, based on which \mathcal{Q}_I , \mathcal{Q}_C and \mathcal{Q}_L can be determined. For example, the symbol indexes for 16QAM is shown in Fig. 4 (a1), and we have

$$\begin{aligned}\mathcal{Q}_I &= \{0, 4, 8, 12\}, \mathcal{Q}_C = \{2, 6, 10, 14\}, \\ \mathcal{Q}_L &= \{1, 3, 5, 7, 9, 11, 13, 15\}.\end{aligned}\quad (23)$$

For PSK, we define $v_q = \exp[j(q + \frac{1}{2})\frac{2\pi}{Q}]$, $\forall q \in \mathcal{Q}$, and $\mathcal{Q}_C = \mathcal{Q}$.

The Gaussian variance is estimated from the received signals belonging to inner symbols, i.e.,

$$\hat{\sigma}_{is}^2 = \frac{1}{\sum_{q \in \mathcal{Q}_I} L_q} \sum_{q \in \mathcal{Q}_I} \sum_{l=1}^{L_q} \|\mathbf{y}_q^p[l] - \mathbf{v}_q\|_2^2. \quad (24)$$

The likelihood functions in the modified Gaussian soft demodulator have the same formulation as the conventional soft

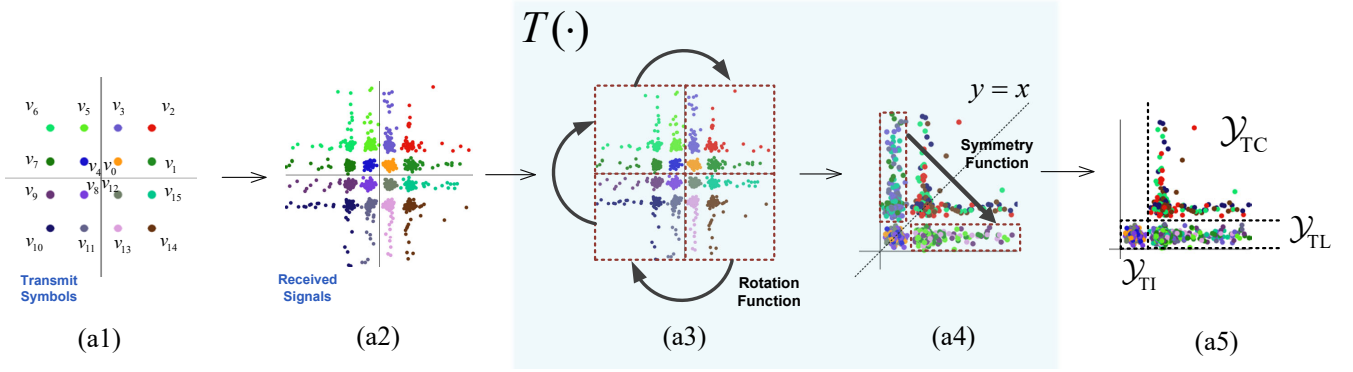


Fig. 4. The constructions of \mathcal{Y}_{TI} , \mathcal{Y}_{TC} , and \mathcal{Y}_{TL} for 16QAM. The correspondence between the colors of received signals and the transmit symbols implies that the corresponding transmit symbols for each signal is known to the UE.

demodulator (10) while replacing $\hat{\sigma}_s^2$ with $\hat{\sigma}_{is}^2$.

B. GMM Soft Demodulator

The modified Gaussian soft demodulator still faces challenges in computing LLRs for received signals belonging to **Type II**, where the distribution of QAM signals or PSK received signals without rescaling deviates significantly from a Gaussian distribution. Although the distribution of rescaled PSK received signals may be approximated by a Gaussian distribution, such as the received signals in (16) from CISB and CIMMSE, the modified Gaussian soft demodulator still cannot be applied due to $\mathcal{Q}_I = \emptyset$ in PSK. To address this issue, we design the GMM soft demodulator, which employs GMM to approximate $f_Y(\mathbf{y}|\mathbf{v}_q)$ from received pilot signals.

GMM is a mixture of several Gaussian distributions, and its PDF for 2D samples is given by [41]

$$f_g(\mathbf{y}; \mathcal{P}) = \sum_{n=1}^{N_g} a_n \frac{\exp\left[-\frac{(\mathbf{y}-\boldsymbol{\mu}_n)^T \boldsymbol{\Sigma}_n^{-1} (\mathbf{y}-\boldsymbol{\mu}_n)}{2}\right]}{2\pi \cdot \det(\boldsymbol{\Sigma}_n)^{\frac{1}{2}}}, \quad (25)$$

where N_g denotes the order of GMM. The parameters of the GMM are given by $\mathcal{P} = \{\boldsymbol{\mu}_n, \boldsymbol{\Sigma}_n, a_n\}_{n=1}^{N_g}$, where $\boldsymbol{\mu}_n \in \mathbb{R}^{2 \times 1}$, $\boldsymbol{\Sigma}_n \in \mathbb{R}^{2 \times 2}$, and $a_n \in \mathbb{R}$ denote expectation, covariance, and weight of n -th Gaussian distribution, respectively. GMM can be used to approximate a certain distribution, i.e., there exist Q GMMs satisfying

$$f_Y(\mathbf{y}|\mathbf{v}_q) \approx f_g(\mathbf{y}; \mathcal{P}_q), \quad \forall q \in \mathcal{Q}, \quad (26)$$

where \mathcal{P}_q denotes the GMM parameters for $f_Y(\mathbf{y}|\mathbf{v}_q)$. Thus, PDF $f_Y(\mathbf{y}|\mathbf{v}_q)$ can be obtained by finding the best-matched \mathcal{P}_q . As the signals in \mathcal{Y}_q are discrete samples of $f_Y(\mathbf{y}|\mathbf{v}_q)$, \mathcal{P}_q can be estimated by certain estimation algorithm $C(\cdot)$ as [42]

$$\hat{\mathcal{P}}_q = C(\mathcal{Y}_q), \quad \forall q \in \mathcal{Q}. \quad (27)$$

Since the number of unknown parameters is increasing with the number of PDFs to be estimated, it requires a larger L_q to obtain accurate estimates of these unknown parameters, which introduces a significant pilot overhead. Thus, how to reduce the number of PDFs to be estimated by revealing the correlation

between received symbols is a crucial issue in GMM soft demodulators.

Proposition 1: For PSK and 16QAM transmission with SLP schemes CISB, CIMMSE or ASM, $f_Y(\mathbf{y}|\mathbf{v}_m)$ and $f_Y(\mathbf{y}|\mathbf{v}_n)$ are related as follows

$$f_Y(\mathbf{y}|\mathbf{v}_m) = f_Y(R_{m-n}(\mathbf{y})|\mathbf{v}_n), \quad m, n \in \mathcal{Q}, \quad (28)$$

where m and n should satisfy $\frac{m-n}{4} \in \mathbb{Z}$ for 16QAM transmission. $R_t(\cdot)$, $t \in \mathbb{N}$ is the rotation function defined as

$$R_t\left(\begin{bmatrix} \Re(\bar{y}) \\ \Im(\bar{y}) \end{bmatrix}\right) = \begin{bmatrix} \Re\left(\bar{y} \cdot \exp\left(-jt\frac{2\pi}{Q}\right)\right) \\ \Im\left(\bar{y} \cdot \exp\left(-jt\frac{2\pi}{Q}\right)\right) \end{bmatrix}. \quad (29)$$

Proof: See Appendix A.

Remark 1: The above proposition indicates that the received signal density of \mathbf{v}_m can be rotated into that of \mathbf{v}_n . Following this proposition, $\{f_Y(\mathbf{y}|\mathbf{v}_q)\}_{q \in \mathcal{Q}}$ of PSK and QAM transmission can be respectively obtained from $f_Y(\mathbf{y}|\mathbf{v}_0)$ and $\{f_Y(\mathbf{y}|\mathbf{v}_q)\}_{q \in \{0,1,2,3\}}$ by utilizing $R_t(\cdot)$, which significantly reduces the number of parameters to be estimated.

For 16QAM transmission, we further make the approximation that the received signal distributions of \mathbf{v}_1 and \mathbf{v}_3 are symmetric about the line $y=x$, i.e.,

$$f_Y(\mathbf{y}|\mathbf{v}_1) = f_Y(S(\mathbf{y})|\mathbf{v}_3), \quad (30)$$

where $S(\cdot)$ is the symmetry function defined as

$$S\left(\begin{bmatrix} \Re(\bar{y}) \\ \Im(\bar{y}) \end{bmatrix}\right) = \begin{bmatrix} \Im(\bar{y}) \\ \Re(\bar{y}) \end{bmatrix}. \quad (31)$$

Therefore, only $\{f_Y(\mathbf{y}|\mathbf{v}_q)\}_{q \in \{0,1,2\}}$ requires to be estimated. Since $f_Y(\mathbf{y}|\mathbf{v}_0)$, $f_Y(\mathbf{y}|\mathbf{v}_1)$, and $f_Y(\mathbf{y}|\mathbf{v}_2)$ respectively contain the distribution properties of the received signals belonging to the inner, corner, and lateral constellation points, we use $f_{Y_I}(\mathbf{y})$, $f_{Y_C}(\mathbf{y})$, and $f_{Y_L}(\mathbf{y})$ to denote them. Combining **Proposition 1** and (30), we have

$$f_Y(\mathbf{y}|\mathbf{v}_q) = \begin{cases} f_{Y_I}(T(\mathbf{y}, q)), & \text{if } q \in \mathcal{Q}_I \\ f_{Y_C}(T(\mathbf{y}, q)), & \text{if } q \in \mathcal{Q}_C \\ f_{Y_L}(T(\mathbf{y}, q)), & \text{if } q \in \mathcal{Q}_L \end{cases}, \quad (32)$$

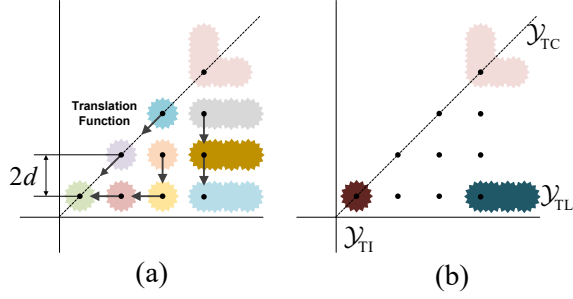


Fig. 5. The constructions of \mathcal{Y}_{TI} , \mathcal{Y}_{TC} , and \mathcal{Y}_{TL} for 64QAM (The process of Fig.4 (a1)-(a4) is omitted). d is half of the distance between adjacent constellation points.

where $T(\cdot)$ is the transform function given by

$$T(\mathbf{y}, q) = \begin{cases} S(R_{4\lfloor \frac{q}{4} \rfloor}(\mathbf{y})), & \text{if } q \in \{3, 7, 11, 15\} \\ R_{4\lfloor \frac{q}{4} \rfloor}(\mathbf{y}), & \text{otherwise} \end{cases}. \quad (33)$$

Given certain sample $\mathbf{y}_m^p[l]$ from $f_Y(\mathbf{y}|\mathbf{v}_m)$, $T(\mathbf{y}_m^p[l])$ can be seen as the sample from $f_Y(\mathbf{y}|\mathbf{v}_n)$ if the received signal distribution of \mathbf{v}_m can be transformed into that of \mathbf{v}_n by $T(\cdot)$, i.e., $f_Y(\mathbf{y}|\mathbf{v}_m) = f_Y(T(\mathbf{y})|\mathbf{v}_n)$. Thus, we define

$$\mathcal{Y}_{TI} = \left\{ T(\mathbf{y}_q^p, q) \mid \mathbf{y}_q^p \in \bigcup_{q' \in \mathcal{Q}_I} \mathcal{Y}_{q'} \right\}, \quad (34)$$

where \mathcal{Y}_{TC} and \mathcal{Y}_{TL} can be obtained in a similar manner by replacing \mathcal{Q}_I with \mathcal{Q}_C and \mathcal{Q}_L . \mathcal{Y}_{TI} , \mathcal{Y}_{TC} , and \mathcal{Y}_{TL} can be seen as the samples from $f_{Y_I}(\mathbf{y})$, $f_{Y_C}(\mathbf{y})$, and $f_{Y_L}(\mathbf{y})$ respectively. The construction of these three sets is shown in Fig. 4 (a1)-(a5). Then, we use GMM to approximate the three probability density functions. We illustrate the process with $f_{Y_I}(\mathbf{y})$ as an instance:

$$f_{Y_I}(\mathbf{y}) \approx f_g(\mathbf{y}; \mathcal{P}_I), \quad \hat{\mathcal{P}}_I = C(\mathcal{Y}_{TI}). \quad (35)$$

Due to the increased number of inner and lateral constellation points in higher-order QAM, $R_t(\cdot)$ and $S(\cdot)$ alone are insufficient. Therefore, we further introduce the translation function depicted in Fig. 5 for $T(\cdot)$. Fig. 5 (a) shows the signal distributions after process of Fig.4 (a1)-(a4). Received signals are then translated based on the relative positions of the corresponding transmit symbols so as to merge the received signals belonging to the inner and lateral symbols, respectively, as shown in Fig. 5 (b). We omit the mathematical definition of the translation function due to space limitations.

For PSK transmission, formulation (32) and (34) are also capable, where $\mathcal{Q}_I = \mathcal{Q}_L = \emptyset$. f_{Y_C} denotes $f_Y(\mathbf{y}|\mathbf{v}_0)$ and

$$T(\mathbf{y}, q) = R_q(\mathbf{y}), \quad \forall q \in \mathcal{Q}. \quad (36)$$

For the same L_P , the performance of $C(\cdot)$ in (35) is much better than that in (27) since the numbers of samples in \mathcal{Y}_{TI} , \mathcal{Y}_{TC} , and \mathcal{Y}_{TL} are $|\mathcal{Q}_I|$, $|\mathcal{Q}_C|$, and $|\mathcal{Q}_L|$ times greater than that of \mathcal{Y}_q in (27). By defining $\hat{f}_Y(\mathbf{y}^d[l]|\mathbf{v}_q)$ and $\widehat{\text{LLR}}_i[l]$ as the estimation of $f_Y(\mathbf{y}^d[l]|\mathbf{v}_q)$ and the LLR belonging to i -th bit of $\mathbf{y}^d[l]$, the GMM soft demodulator is presented in Algorithm 1, which is also capable for PSK by setting $\mathcal{Q}_I =$

Algorithm 1 GMM Soft Demodulator

```

1: Input:  $\mathcal{Q}_I, \mathcal{Q}_L, \mathcal{Q}_C, \{\mathcal{Y}_q\}_{q \in \mathcal{Q}}, \mathbf{Y}_d$ .
2: Get  $\mathcal{Y}_{TI}, \mathcal{Y}_{TC}$ , and  $\mathcal{Y}_{TL}$  using (34).
3: Estimate GMM parameters:
    $\hat{\mathcal{P}}_I = C(\mathcal{Y}_{TI}), \hat{\mathcal{P}}_C = C(\mathcal{Y}_{TC}), \hat{\mathcal{P}}_L = C(\mathcal{Y}_{TL})$ .
4: for  $l = 1$  to  $L_D$  do
5:   for  $q = 0$  to  $Q - 1$  do
6:      $\hat{f}_Y(\mathbf{y}^d[l]|\mathbf{v}_q) = \begin{cases} f_g(T(\mathbf{y}^d[l], q) | \hat{\mathcal{P}}_I) & \text{if } q \in \mathcal{Q}_I \\ f_g(T(\mathbf{y}^d[l], q) | \hat{\mathcal{P}}_C) & \text{if } q \in \mathcal{Q}_C \\ f_g(T(\mathbf{y}^d[l], q) | \hat{\mathcal{P}}_L) & \text{if } q \in \mathcal{Q}_L \end{cases}$ 
7:   end for
8:   for  $i = 1$  to  $\log_2 Q$  do
9:      $\widehat{\text{LLR}}_i[l] = \ln \frac{\sum_{\mathbf{v}_q \in \mathcal{S}_i^+} \hat{f}_Y(\mathbf{y}^d[l]|\mathbf{v}_q)}{\sum_{\mathbf{v}_q \in \mathcal{S}_i^-} \hat{f}_Y(\mathbf{y}^d[l]|\mathbf{v}_q)}$ 
10:  end for
11: end for
12: Output:  $\{\widehat{\text{LLR}}_i[l]\}_{i=1}^{\log_2 Q}, \forall l = 1, \dots, L_D$ .

```

$$\mathcal{Q}_L = \mathcal{Y}_{TI} = \mathcal{Y}_{TL} = \emptyset.$$

C. Pilot Feature Extraction Network

To further reduce the pilot overhead, we propose PFEN, a low-complexity demodulator that utilizes the feature extraction block (FEB) to extract the signal distribution features from \mathcal{Y}_{TI} , \mathcal{Y}_{TC} , and \mathcal{Y}_{TL} . Since elements in these three sets are order-independent, FEB is expected to be a permutation-invariant function [43], which can be achieved by the outstanding transformer-based operations [44]. The structure of PFEN is shown in Fig. 6, where three FEBs are used to process \mathcal{Y}_{TI} , \mathcal{Y}_{TC} , and \mathcal{Y}_{TL} individually. Note that the transformer-based operations are also well-suitable for pilot signals with adjustable lengths in practical communication systems since their pre-trained model can deal with varying numbers of inputs [45].

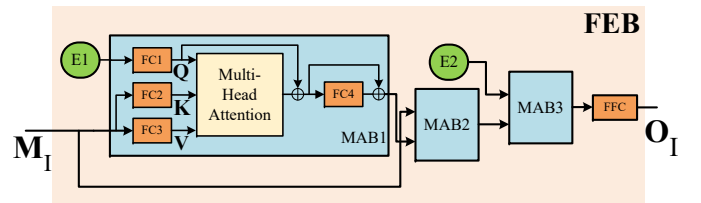


Fig. 6. Structure of FEB.

1) *FEB*: Since the structure of three FEBs for \mathcal{Y}_{TI} , \mathcal{Y}_{TC} , and \mathcal{Y}_{TL} are the same, we only introduce the one for \mathcal{Y}_{TI} . The parameters of the FEB for \mathcal{Y}_{TI} are listed in Table I: ‘Heads Number’ represents the number of heads of ‘Multi Head Attention’ module [46]; ‘FC’ and ‘FFC’ denote fully connected layer applied at the last dimension; \mathbf{E}_1 and \mathbf{E}_2 are trainable matrices introduced for reducing the dimension of variables involved in computation [44]; \mathbf{M}_I and \mathbf{O}_I are the input and output. Except for the received pilot signals, we also

TABLE I
NETWORK STRUCTURE AND MAJOR PARAMETERS OF SUBMODEL FOR \mathcal{Y}_I

	MAB			FC Size	Matrix Size	
	MAB1	MAB2	MAB2	FFC	\mathbf{E}_1	\mathbf{E}_2
Heads Number	4	4	4	32×6	16×32	$N_g \times 32$
FC1 Size	32×32	4×32	32×32		\mathbf{M}_I	\mathbf{O}_I
FC2/3 Size	4×32	32×32	32×32		$L_I \times 3$	$N_g \times 6$
FC4 Size	32×32	32×32	32×32			

choose $\bar{\gamma}$ as the input to provide more information for PFEN. The input matrix \mathbf{M}_I is given by

$$\begin{aligned} \mathbf{M}_I &= [\mathbf{m}[1]^T, \mathbf{m}[2]^T, \dots, \mathbf{m}[L_I]^T]^T \in \mathbb{R}^{L_I \times 3}, \\ \mathbf{m}[l] &= [\mathbf{y}_{\text{TI}}^p[l]^T, \bar{\gamma}] \in \mathbb{R}^{1 \times 3}, l = 1, \dots, L_I, \end{aligned} \quad (37)$$

where $\mathbf{y}_{\text{TI}}^p[l]$ denotes l -th signal in \mathcal{Y}_{TI} , and $L_I = |\mathcal{Y}_{\text{TI}}|$.

The parameters in the n -th Gaussian distribution can be expressed as

$$\alpha_n, \boldsymbol{\mu} = \begin{bmatrix} \mu_{n,1} \\ \mu_{n,2} \end{bmatrix}, \boldsymbol{\Sigma}_n = \begin{bmatrix} \sigma_{n,1}^2 & \sigma_{n,2}^2 \\ \sigma_{n,2}^2 & \sigma_{n,3}^2 \end{bmatrix}, \quad (38)$$

which contains 6 parameters. Denote the output as $\mathbf{O}_I \in \mathbb{R}^{N_g \times 6}$, and the process of FEB can be expressed as

$$\mathbf{O}_I = \text{FEB}_I(\mathbf{M}_I). \quad (39)$$

Due to the permutation invariance of FEB, rows of \mathbf{O}_I and \mathbf{M}_I are unordered, which means \mathbf{O}_I and \mathbf{M}_I can be regarded as two sets with their rows as elements.

2) *GPL*: We design a GMM property layer (GPL) to ensure that the outputs meet the required properties of GMM parameters, i.e.,

$$\hat{\mathcal{P}}_I = \text{GPL}(\mathbf{O}_I). \quad (40)$$

GPL performs the following operations:

- **Weight**: To keep $\sum_{n=1}^{N_g} a_n = 1$, GPL applies

$$\hat{a}_1, \dots, \hat{a}_{N_g} = \text{Softmax}(o_{1,1}, \dots, o_{N_g,1}), \quad (41)$$

where $o_{i,j}$ is the (i,j) -th element of \mathbf{O}_I .

- **Mean**: $\hat{\boldsymbol{\mu}}_n = [o_{n,2}, o_{n,3}]^T$, $n = 1, \dots, N_g$.
- **Covariance**: To keep $\hat{\boldsymbol{\Sigma}}_n$ positive-definite and its diagonal elements non-negative, GPL applies

$$\begin{aligned} \hat{\sigma}_{n,1}^2 &= \text{SoftPlus}(o_{n,4}), \quad \hat{\sigma}_{n,3}^2 = \text{SoftPlus}(o_{n,6}), \\ \hat{\sigma}_{n,2}^2 &= \sqrt{\hat{\sigma}_{n,1}^2 \hat{\sigma}_{n,3}^2} \cdot \text{Tanh}(o_{n,5}), \quad n = 1, \dots, N_g. \end{aligned} \quad (42)$$

3) *Loss Function*: To facilitate the computation of the loss function during training, we also separate \mathbf{Y}_d according to (22) and apply $T(\cdot)$ to transform the separated sets into $\mathcal{Y}_{\text{TI}}^d$, $\mathcal{Y}_{\text{TC}}^d$, and $\mathcal{Y}_{\text{TL}}^d$ like (34). Similar but not identical to the ML criterion that tries to maximize the log-likelihood function of samples, we hope the parameter extracted from \mathcal{Y}_{TI} could maximize the likelihood of $\mathcal{Y}_{\text{TI}}^d$. This idea ensures parameters extracted from the received pilot signals are optimized to match the received

Algorithm 2 PFEN Soft Demodulator

- 1: **Input**: $\mathcal{Q}_I, \mathcal{Q}_L, \mathcal{Q}_C, \{\mathcal{Y}_q\}_{q \in \mathcal{Q}}, \mathbf{Y}_d, \bar{\gamma}$.
- 2: Get $\mathcal{Y}_{\text{TI}}, \mathcal{Y}_{\text{TC}}$, and \mathcal{Y}_{TL} using (34).
- 3: Get $\mathbf{M}_I, \mathbf{M}_C$, and \mathbf{M}_L using (37).
- 4: $\mathbf{O}_I = \text{FEB}_I(\mathbf{M}_I)$, $\hat{\mathcal{P}}_I = \text{GPL}(\mathbf{O}_I)$.
- 5: $\mathbf{O}_C = \text{FEB}_C(\mathbf{M}_C)$, $\hat{\mathcal{P}}_C = \text{GPL}(\mathbf{O}_C)$.
- 6: $\mathbf{O}_L = \text{FEB}_L(\mathbf{M}_L)$, $\hat{\mathcal{P}}_L = \text{GPL}(\mathbf{O}_L)$.
- 7: The same as the steps 4-11 in Algorithm 1.
- 8: **Output**: $\{\widehat{\text{LLR}}_i[l]\}_{i=1}^{\log_2 Q}$, $\forall l = 1, \dots, L_D$.

data signals, and the loss function is designed as

$$\begin{aligned} \text{Loss}_I &= \\ &= -\mathbb{E}_{\mathcal{Y}_{\text{TI}}^d} \left[\ln \sum_{n=1}^{N_g} \hat{a}_n \frac{\exp \left[-\frac{(\mathbf{y}_{\text{TI}}^d - \hat{\boldsymbol{\mu}}_n)^T \hat{\boldsymbol{\Sigma}}_n^{-1} (\mathbf{y}_{\text{TI}}^d - \hat{\boldsymbol{\mu}}_n)}{2} \right]}{2\pi \det(\hat{\boldsymbol{\Sigma}}_n)^{\frac{1}{2}}} \right], \end{aligned} \quad (43)$$

where \mathbf{y}_{TI}^d is the sample in $\mathcal{Y}_{\text{TI}}^d$.

PFEN for PSK has a similar structure and training process to those for QAM. Their difference is that PFEN for PSK only needs a FEB due to $\mathcal{Y}_{\text{TI}} = \mathcal{Y}_{\text{TL}} = \emptyset$. For the received signals without power allocation and rescaling, $\bar{\gamma}$ is removed from the input (37).

V. NUMERICAL RESULTS

In this section, we use the Monte Carlo method to evaluate the performance of the proposed methods in the scenario of an MU-MISO system and Rayleigh fading channel. Unless otherwise specified, we set $P_{\text{T}}[l] = 1$ and $\text{SNR} = \frac{1}{\sigma^2}$. We consider the conventional ZF precoding scheme and three SLP schemes, CISB [7], [15], CIMMSE [39], and ASM [40]. The proposed demodulators are compared with the Gaussian demodulator and the demodulator based on the Class A model in [29], denoted as ‘CA’. For CA, the estimation method of power parameter σ_A^2 is the same as the Gaussian demodulator, and the term number is set to $M_{\text{ca}} = 20$ [29].

A. Training Details and Complexity Analysis

1) *Training Details*: The training details of PFEN are as follows. To improve the diversity of the dataset, we record $\mathbf{h}^T \mathbf{x}[l]$ instead of $\mathbf{h}^T \mathbf{x}[l] + n[l]$ and generate noise randomly at the training phase. The size of the training dataset for $\mathbf{h}^T \mathbf{x}[l]$ is

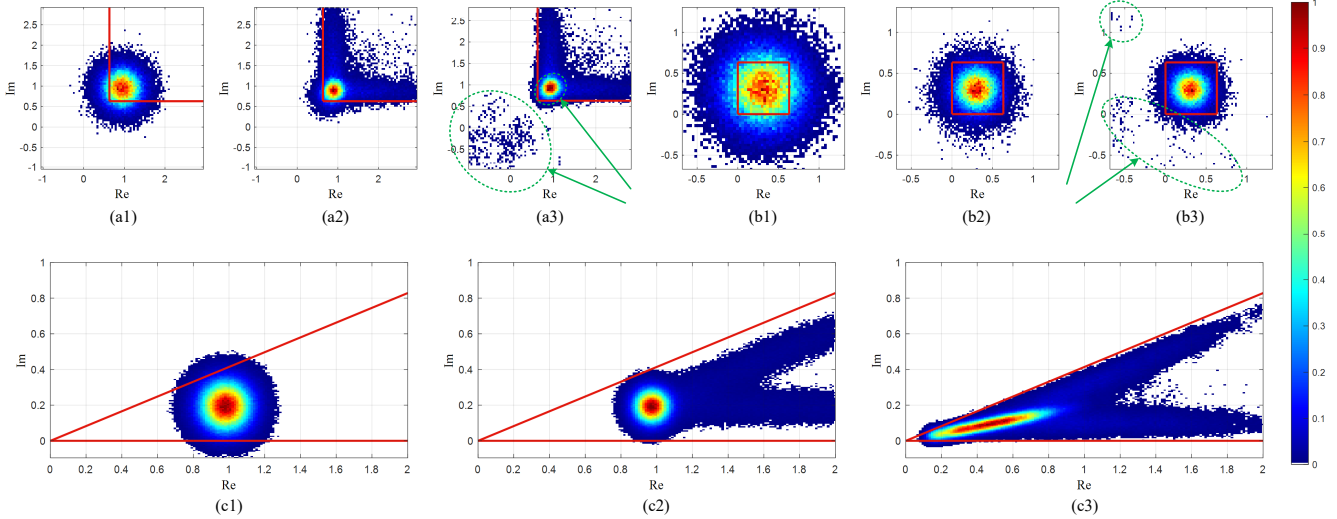


Fig. 7. Normalized $f_Y(\mathbf{y}[l]|\mathbf{v}_q)$ where \mathbf{v}_q is (a1) corner 16QAM constellation point, ZF. (a2) corner 16QAM constellation point, CIMMSE. (a3) corner 16QAM constellation point, ASM. (b1) inner 16QAM constellation point, ZF. (b2) inner 16QAM constellation point, CIMMSE. (b3) inner 16QAM constellation point, ASM. (c1) 16PSK constellation point, ZF, WR. (c2) 16PSK constellation point, CIMMSE, WR. (c3) 16PSK constellation point, CIMMSE, WOR. $N = K = 8$, $\text{SNR} = \frac{P}{\sigma^2}$ is 20dB, the red lines represent the decision boundaries of the constellation points.

[300, N_{SNR} , K , $L_P + L_D$, 2], which contains 300 channels, the scenarios of N_{SNR} different SNR values, and K UEs. It should be noted that PFEN is trained to work in full SNR ranges, and the training data is not used for performance evaluation. For each channel, SNR, and UE, the received signals are stored as real and imaginary parts, and the first $L_P = 1024$ or 128 (resp. QAM or PSK) signals are \mathbf{Y}_p , and the latter $L_D = 2048$ signals are \mathbf{Y}_d . For the convenience of batch computing, we set $L_q = L_P/Q$, $\forall q \in Q$ when training, while they can be unequal for validation since the amount of input samples is adjustable for a pre-trained transformer module. Similarly, L_P can be flexibly adjusted, and L_D could be expanded to be much larger when PFEN is employed in practical systems. We adopt the Adam optimizer with the learning rate progressively decreasing from 10^{-4} to 10^{-6} , respectively. The number of iterations and batch size are set to be 90000 and 32.

2) *Computational Complexity of GMM Soft Demodulator:* Since the prior information about the signal distribution is unknown, we choose the ML criterion instead of the MAP criterion for parameter estimation [47], [48]. Based on such criterion, we employed the EM algorithm as $C(\cdot)$, which is an efficient parameter estimation algorithm commonly used for GMM [49], [50]. The complexity of **Algorithm 1** is dominated by estimating \hat{P}_I , \hat{P}_C , and \hat{P}_L (step 3), as well as the LLR computation (steps 5-10). The computational complexity of

the former (EM algorithm) is $\mathcal{O}(N_g L_P)$ in every iteration. For each $\mathbf{y}^d[l]$, steps 5-10 have a complexity order of $\mathcal{O}(N_g Q)$. The computational complexities of GMM is summarized in Table II, where the number of iterations is denoted by η_g . Specifically, we set $N_g = 5$ for the GMM in PFEN and GMM soft demodulators.

3) *Computational Complexity of PFEN Soft Demodulator:* We denote D_{SA} and N_H as the last dimension of $\mathbf{Q}/\mathbf{K}/\mathbf{V}$ and the number of heads in FEB. The dimensions of the matrices \mathbf{E}_1 , \mathbf{E}_2 , and \mathbf{M} are represented by $N_{\mathbf{E}_1} \times D_{\text{SA}}$, $N_g \times D_{\text{SA}}$, and $L_P \times D_M$. Given $N_{\mathbf{E}_1} \gg N_g$, the four full connection layer in FEB have the complexity of $\mathcal{O}(N_{\mathbf{E}_1} D_{\text{SA}}^2 + L_P D_M D_{\text{SA}})$. ‘Multi-Head Attention’ module has the complexity order of $\mathcal{O}(N_{\mathbf{E}_1} D_{\text{SA}} L_P)$ [46]. Thus, PFEN soft demodulator computes \hat{P}_I , \hat{P}_C , and \hat{P}_L with complexity of $\mathcal{O}(L_P (D_M D_{\text{SA}} + N_{\mathbf{E}_1} D_{\text{SA}}) + N_{\mathbf{E}_1} D_{\text{SA}}^2)$. According to Table I, the parameter dimensions are set as $D_{\text{SA}} = 32$, $N_H = 4$, $N_{\mathbf{E}_1} = 16$.

The computational complexities of soft demodulators are summarized in Table II, where the number of iterations in CA is denoted by η_{ca} . The computational complexity of LLR computation (steps 4-11 in **Algorithm 1**) is ignored since it depends on L_D and is relatively smaller compared to that of estimations, and the demodulation performance is

TABLE II
COMPUTATIONAL COMPLEXITIES OF SOFT DEMODULATORS

Demodulator	QAM			PSK			Demodulator	Complexity Order
	CA	GMM	PFEN	CA	GMM	PFEN		
Number of Multiplications (10^5)	677.64	116.85	37.85	80.48	8.75	5.45	CA	$\mathcal{O}(\eta_{\text{ca}} L_P M_{\text{ca}})$
Execution Time (ms)	539.52	82.27	5.76	132.01	9.80	1.69	GMM	$\mathcal{O}(\eta_g L_P N_g)$
							PFEN	$\mathcal{O}(L_P D_{\text{SA}} (D_M + N_{\mathbf{E}_1}) + D_{\text{SA}}^2 N_{\mathbf{E}_1})$

determined by \widehat{P}_1 , \widehat{P}_C , and \widehat{P}_L . Note that

$$L_P > \eta_{ca} > \eta_g \gg D_{SA} > M_{ca} > N_{E_1} > N_g \geq D_M. \quad (44)$$

The average number of multiplications is computed with $N = K = 8$ and $N_g = 5$, and the average execution time is evaluated on Intel Xeon W-2150B CPU (3.00GHz). The configuration of QAM and PSK are 1) ASM precoder, 16QAM, $L_P = 1024$, and SNR = 0, 5, ..., 40; 2) CISB-PA precoder, 16PSK, $L_P = 128$, and SNR = 0, 5, ..., 40. PFEN has a greater advantage in execution time since it contains no iterative computations.

B. Coded System Performance

In this subsection, we consider the coded system that employs the low-density parity check (LDPC) coding scheme [35]. In this section, **Gaus** and **CA** represent Gaussian and CA soft demodulators, while **MGaus**, **GMM**, and **PFEN** represent the modified Gaussian, GMM, and PFEN demodulators proposed in Sections IV-A, IV-B, and IV-C, respectively. Since L_P (the number followed by the demodulator in the legends) has little impact on **Gaus** and **MGaus**, the simulation focuses on the effect of L_P on **GMM** and **PFEN**. Except for the spectrum efficiency³, we use the mutual information (MI) between the coded bits **B** and the corresponding LLR, which is approximated using the following formulation, to comprehensively evaluate the performance of the SLP transceivers [51], [52].

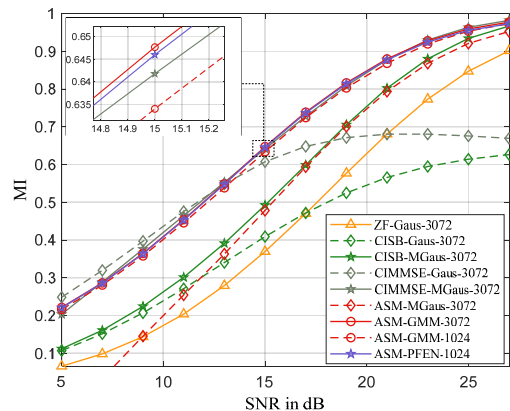
$$I(\mathbf{B}; \mathbf{LLR}) \approx 1 - \frac{1}{L_D \cdot \log_2 Q} \sum_{l=1}^{L_D} \sum_{i=1}^{\log_2 Q} \log_2 \left[1 + \exp \left(-b_i[l] \cdot \widehat{LLR}_i[l] \right) \right], \quad (45)$$

where $b_i[l]$ denotes the i -th coded bit of $\mathbf{y}[l]$.

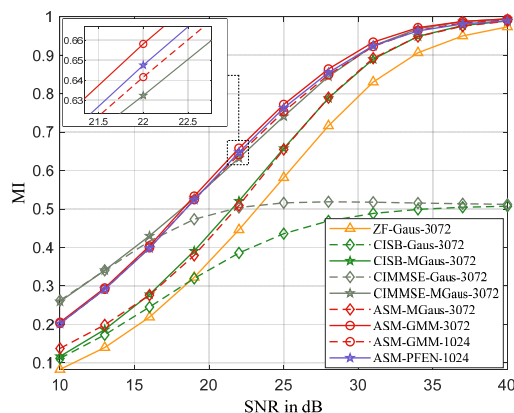
Fig. 7 shows the normalized $f_Y(\mathbf{y}[l]|\mathbf{v}_q)$ with ZF, CIMMSE, and ASM precodings. Different from the circular density plot of the Gaussian distribution, the ASM exhibits an elliptical distribution center in Fig.7 (a3), and there are scattered irregular points away from the decision region in both Fig.7 (a3) and (b3), which can impact the demodulation of the received signals.

Fig. 8(a) and Fig. 8(b) compare MI performance between different transceivers. Compared with CIMMSE-Gaus-3072, which levels off at about 0.65 for 16QAM and further degrades for 64QAM, the MI of CIMMSE-MGaus-3072 shows significant improvement, reaching 1.00 at higher SNR values. The similar trend can also be observed from the performance of CISB with demodulators. The performance of transceiver ASM-PFEN-1024 is almost the same as ASM-GMM-3072, which indicates that **PFEN** can effectively reduce the pilot overhead. When MI = 0.5 in scenarios $N = K = 8$ with 16QAM and $N = K = 12$ with 64QAM, ASM-GMM-1024 transceiver provides SNR gains of about 2.7dB and 3.7dB than ASM-MGaus-3072, and ASM-PFEN-1024 transceiver provides SNR gains of about 3.1dB and 4.0dB. The performance gap between the **GMM** and **MGaus** demodulators

³The computation method of spectrum efficiency refers to Section IV in [39].



(a) 16QAM, $N = K = 8$.



(b) 64QAM, $N = K = 12$.

Fig. 8. MI vs SNR, QAM, $L_D = 2048$.

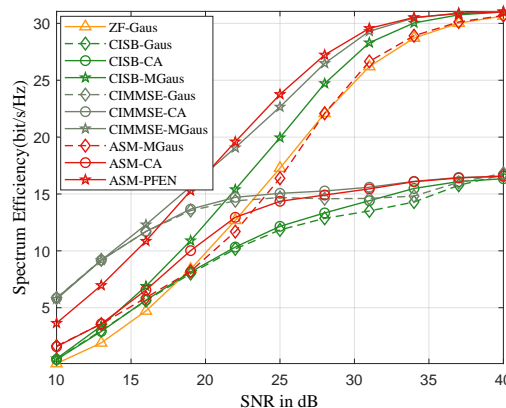
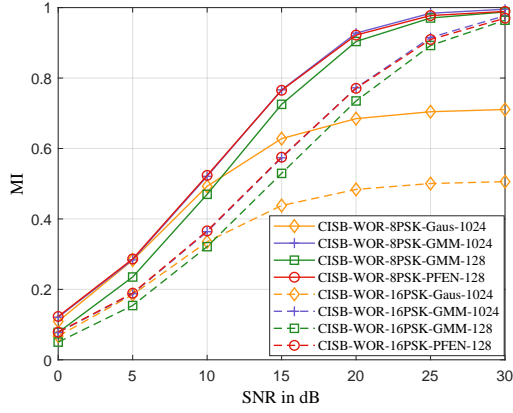


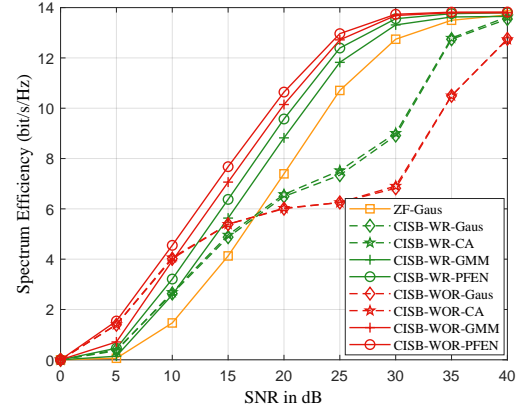
Fig. 9. Spectrum Efficiency vs SNR, 64QAM, $N = K = 12$, $L_P = 1024$, $L_D = 2048$, LDPC.

under the ASM scheme illustrates the significant impact of non-Gaussian signals from ASM on the LLR calculation of **MGaus**. Due to the similar performance of **CA** to **Gaus** and the abundance of curves, we have omitted the MI performance of **CA** in Fig. 8 for readability.

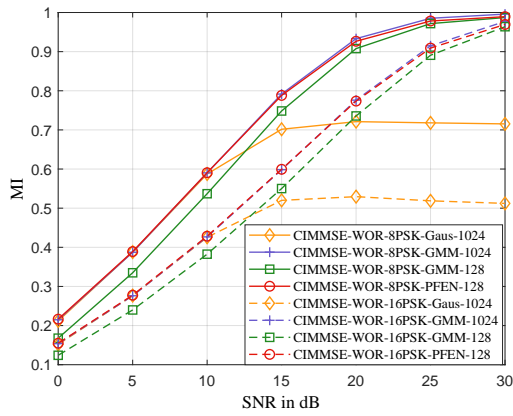
Fig. 9 shows a comparison of the spectrum efficiency for



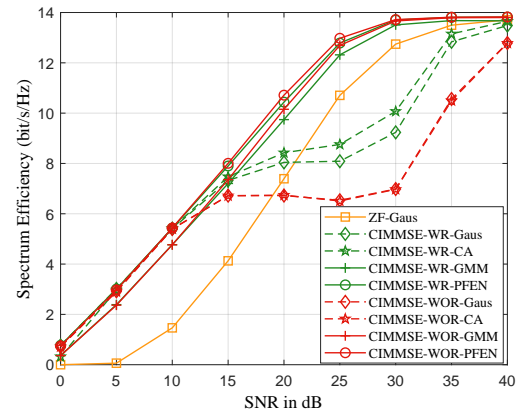
(a) CIBS, WOR.



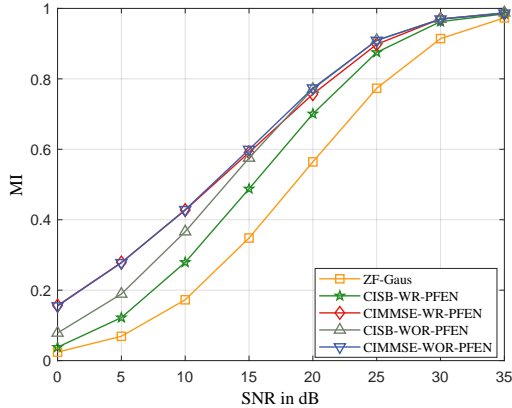
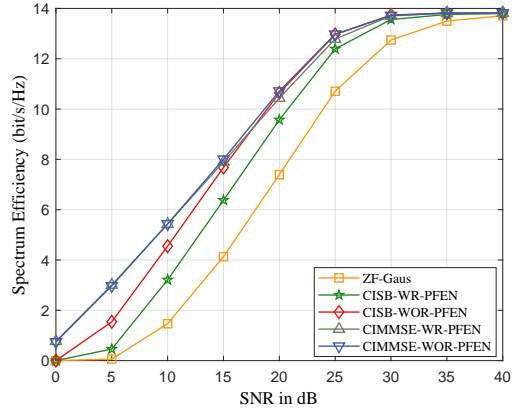
(a) CIBS.



(b) CIMMSE, WOR.



(b) CIMMSE.

(c) 16PSK, $L_P = 128$.

(c) 16PSK.

Fig. 10. MI vs SNR, PSK, $N = K = 8$, $L_D = 2048$.Fig. 11. Spectrum Efficiency vs SNR, 16PSK, $N = K = 8$, $L_P = 128$, $L_D = 2048$, LDPC.

64QAM and $N = K = 12$. It is evident that the Gaussian soft demodulator severely limits the performance of CIBS and CIMMSE, while **MGaus** provides outstanding throughput for these schemes. Since **MGaus** does not match the distribution of received signals from ASM, the spectrum efficiency of ASM-PFEN is significantly higher than ASM-MGaus. When the spectrum efficiency is 15 bits/s/Hz, ASM-PFEN provides an SNR gain of about 3.3dB than CIBS-MGaus. Moreover,

ASM-PFEN outperforms CIMMSE-MGaus slightly in high SNR regimes. It is worth noting that the spectrum efficiency and MI performance of a transceiver, such as CIBS-Gaus, may show some differences due to their different sensitivities to LLR distribution. **CA** cannot provide excellent demodulation performance since its model cannot adapt to the signals with SLP, and it also faces the variance estimation issue as **Gaus**.

The MI comparison for PSK transmission is depicted in Fig. 10. In Fig. 10(a), CISB-NPA-Gaus for 8PSK and 16PSK could only reach MI of about 0.72 and 0.51 when SNR is 30dB, while the MIs of **GMM** and **PFEN** grow with the increasing SNR and reach 1.00. When L_P decreases from 1024 to 128, **PFEN** achieves the same performance as **GMM** with $L_P = 1024$, while **GMM** has a significant drop in performance. Since CIMMSE has a similar received signal distribution, the above analysis is also applicable to CIMMSE-NPA in Fig. 10(b). It is shown in Fig. 10(c) that SLP schemes outperform ZF precoding scheme with the help of **PFEN** soft demodulator, where CIMMSE-NPA-FPEN provides a 72% MI gain than ZF-Gaus when SNR is 15dB.

Fig. 11 illustrates the comparison of spectrum efficiency for PSK transmission. The spectrum efficiency of CISB-NPA-Gaus and CISB-PA-Gaus is much lower than ‘ZF-Gaus’ in the high SNR regime. CISB-NPA-PFEN and CISB-PA-PFEN provide spectrum efficiency gains of about 46% and 75% than ZF-Gaus. While CISB-NPA-PFEN has better performance than CISB-PA-PFEN in Fig. 11(a), the performance of CIMMSE-NPA-PFEN and CIMMSE-PA-PFEN in Fig. 11(b) is very similar. In Fig. 11, all these excellent transceivers are compared, and CIMMSE-NPA-PFEN has the highest spectrum efficiency.

VI. CONCLUSION

This paper investigated the non-Gaussian soft demodulator for SLP in a coded MU-MISO system. We first analyzed the non-Gaussian characteristics of both PSK and QAM signals with existing SLP schemes and categorized the non-Gaussian signals into two distinct types. To achieve precise LLR estimation from the two categories of non-Gaussian received signals, we put forward the modified Gaussian and the GMM soft demodulators. Additionally, we proposed the PFEN demodulator based on the transformer mechanism in deep learning, which effectively reduces computational complexity and pilot overhead. Simulation results demonstrated that the proposed soft demodulators significantly enhance the throughput of existing SLPs for both PSK and QAM transmission in coded systems.

APPENDIX A

PROOF OF PROPOSITION 1

Without loss of generality, we present the proof for the case of PSK transmission with CISB. The problem of CISB is given by [15], [16]

$$\begin{aligned} & \max_{\mathbf{x}, \gamma} \gamma \\ & \text{s.t. } \mathbf{h}_k^T \mathbf{x} \in \gamma \cdot \mathcal{D}_k, \forall k \in \mathcal{K}, \\ & \|\mathbf{x}\|_2^2 = P_T. \end{aligned} \quad (46)$$

Given $\{\mathbf{h}_k^T\}_{k=1}^K$ and P_T , the optimal \mathbf{x}^* and γ^* are determined by \mathbf{s} , thus we use $\mathbf{x}^*(\mathbf{s})$ and $\gamma^*(\mathbf{s})$ to denote them. As in Section III, we consider the received signals of k -th UE. According to (1), and (7), \bar{y} is given by

$$\bar{y} = \begin{cases} \frac{\mathbf{h}_k^T \mathbf{x}^*(\mathbf{s})}{\gamma^*(\mathbf{s})} + \frac{n_k}{\gamma}, \text{ WR} \\ \mathbf{h}_k^T \mathbf{x}^*(\mathbf{s}) + n_k, \text{ WOR} \end{cases}. \quad (47)$$

We focus on the proof for the case with power allocation, which can be extended to that without power allocation. Since symbols in \mathcal{V} are transmitted with equal probability, \mathbf{s} follows a discrete uniform distribution with the sample space \mathcal{V}^K . Furthermore, $\mathbf{s}_q, \forall q \in \mathcal{Q}$ is defined as the discrete uniformly distributed variable with the following sample space:

$$\mathcal{S}_q = \{\mathbf{s} | \mathbf{s} \in \mathcal{V}^K, [\mathbf{s}]_k = v_q\}, \forall q \in \mathcal{Q}. \quad (48)$$

We respectively denote \mathbf{s}_m^{SP} and \mathbf{s}_n^{SP} as the observations of \mathcal{S}_m and \mathcal{S}_n . For PSK transmission, it can be proved that the following equation is a bijection between \mathcal{S}_m and \mathcal{S}_n

$$\mathbf{s}_m^{\text{SP}} = \mathbf{s}_n^{\text{SP}} \cdot \exp\left[j(m-n)\frac{2\pi}{Q}\right], \forall m, n \in \mathcal{Q}. \quad (49)$$

The above bijection also holds for m and n satisfying $\frac{m-n}{4} \in \mathbb{Z}$ in 16QAM transmission.

Based on the definition of \mathcal{D}_k and the convexity of problem (46), it can be verified that

$$\mathbf{x}^*(\mathbf{s}_m^{\text{SP}}) = \mathbf{x}^*(\mathbf{s}_n^{\text{SP}}) \cdot \exp\left[j(m-n)\frac{2\pi}{Q}\right], \quad (50)$$

$$\gamma^*(\mathbf{s}_m^{\text{SP}}) = \gamma^*(\mathbf{s}_n^{\text{SP}}), \quad (51)$$

where \mathbf{s}_m^{SP} and \mathbf{s}_n^{SP} are observations satisfying (49). Furthermore, we have

$$\frac{\mathbf{h}_k^T \mathbf{x}^*(\mathbf{s}_m^{\text{SP}})}{\gamma^*(\mathbf{s}_m^{\text{SP}})} = \frac{\mathbf{h}_k^T \mathbf{x}^*(\mathbf{s}_n^{\text{SP}})}{\gamma^*(\mathbf{s}_n^{\text{SP}})} \cdot \exp\left[j(m-n)\frac{2\pi}{Q}\right]. \quad (52)$$

Although the problem of ASM is non-convex, it can be proven the variables after each iteration of Algorithm 1 in [40] satisfy (52).

According to (48), (49), and (52), $\frac{\mathbf{h}_k^T \mathbf{x}^*(\mathbf{s}_m)}{\gamma^*(\mathbf{s}_m)}$ are identically distributed with $\frac{\mathbf{h}_k^T \mathbf{x}^*(\mathbf{s}_n)}{\gamma^*(\mathbf{s}_n)} \cdot \exp\left[j(m-n)\frac{2\pi}{Q}\right]$. Since n_k follow $\mathcal{CN}(0, \sigma^2)$ that is circular symmetric, \bar{y}_m and $\bar{y}_n \cdot \exp\left[j(m-n)\frac{2\pi}{Q}\right]$ are identically distributed, where \bar{y}_m and \bar{y}_n represent \bar{y} with transmit symbol vector \mathbf{s}_m and \mathbf{s}_n , respectively. As $f_Y(\mathbf{y}|\mathbf{v}_q)$ is the PDF of $\begin{bmatrix} \Re(\bar{y}_q) \\ \Im(\bar{y}_q) \end{bmatrix}$, we have

$$f_Y(\mathbf{y}|\mathbf{v}_m) = f_Y(R_{m-n}(\mathbf{y})|\mathbf{v}_n). \quad (53)$$

This concludes the proof.

REFERENCES

- [1] M. Joham, W. Utschick, and J. Nosssek, ‘‘Linear transmit processing in MIMO communications systems,’’ *IEEE Trans. Signal Process.*, vol. 53, no. 8, pp. 2700–2712, Aug. 2005.
- [2] Q. Spencer, A. Swindlehurst, and M. Haardt, ‘‘Zero-forcing methods for downlink spatial multiplexing in multiuser MIMO channels,’’ *IEEE Trans. Signal Process.*, vol. 52, no. 2, pp. 461–471, Febr. 2004.
- [3] A. Bourdoux and N. Khaled, ‘‘Joint TX-RX optimisation for MIMO-SDMA based on a null-space constraint,’’ in *IEEE Veh. Technol. Conf.*, vol. 1, Vancouver, BC, Canada, Sept. 2002, pp. 171–174 vol.1.
- [4] C. Peel, B. Hochwald, and A. Swindlehurst, ‘‘A vector-perturbation technique for near-capacity multiantenna multiuser communication-part I: Channel inversion and regularization,’’ *IEEE Trans. Commun.*, vol. 53, no. 1, pp. 195–202, June 2005.
- [5] M. Alodeh, D. Spano, A. Kalantari, C. G. Tsinos, D. Christopoulos, S. Chatzinotas, and B. Ottersten, ‘‘Symbol-level and multicast precoding for multiuser multiantenna downlink: A state-of-the-art, classification, and challenges,’’ *IEEE Commun. Surv. Tutor.*, vol. 20, no. 3, pp. 1733–1757, May 2018.

- [6] A. Li, D. Spano, J. Krivochiza, S. Domouchtsidis, C. G. Tsinos, C. Masouros, S. Chatzinotas, Y. Li, B. Vucetic, and B. Ottersten, "A tutorial on interference exploitation via symbol-level precoding: Overview, state-of-the-art and future directions," *IEEE Commun. Surv. Tutor.*, vol. 22, no. 2, pp. 796–839, Mar. 2020.
- [7] A. Li, C. Masouros, B. Vucetic, Y. Li, and A. L. Swindlehurst, "Interference exploitation precoding for multi-level modulations: Closed-form solutions," *IEEE Trans. Commun.*, vol. 69, no. 1, pp. 291–308, Jan. 2021.
- [8] C. Masouros and E. Alsusa, "Dynamic linear precoding for the exploitation of known interference in MIMO broadcast systems," *IEEE Trans. Wireless Commun.*, vol. 8, no. 3, pp. 1396–1404, Mar. 2009.
- [9] C. Masouros, "Correlation rotation linear precoding for MIMO broadcast communications," *IEEE Trans. Signal Process.*, vol. 59, no. 1, pp. 252–262, Jan. 2011.
- [10] M. Alodeh, S. Chatzinotas, and B. Ottersten, "A multicast approach for constructive interference precoding in MISO downlink channel," in *IEEE Int. Symp. Inf. Theor. Proc.*, Honolulu, HI, USA, June 2014, pp. 2534–2538.
- [11] C. Masouros and G. Zheng, "Exploiting known interference as green signal power for downlink beamforming optimization," *IEEE Trans. Signal Process.*, vol. 63, no. 14, pp. 3628–3640, Jul. 2015.
- [12] M. Alodeh, S. Chatzinotas, and B. Ottersten, "Constructive interference through symbol level precoding for multi-level modulation," in *IEEE Glob. Commun. Conf. (GLOBECOM)*, San Diego, CA, USA, Dec. 2015, pp. 1–6.
- [13] Y. Liu and W.-K. Ma, "Symbol-level precoding is symbol-perturbed z_f when energy efficiency is sought," in *IEEE Int. Conf. Acoust., Speech Signal Process. (ICASSP)*, Calgary, AB, Canada, Apr. 2018, pp. 3869–3873.
- [14] M. Alodeh, S. Chatzinotas, and B. Ottersten, "Symbol-level multiuser MISO precoding for multi-level adaptive modulation," *IEEE Trans. Wireless Commun.*, vol. 16, no. 8, pp. 5511–5524, Aug. 2017.
- [15] A. Li and C. Masouros, "Interference exploitation precoding made practical: Optimal closed-form solutions for PSK modulations," *IEEE Trans. Wireless Commun.*, vol. 17, no. 11, pp. 7661–7676, Sept. 2018.
- [16] A. Haqiqatnejad, F. Kayhan, and B. Ottersten, "Constructive interference for generic constellations," *IEEE Signal Process. Lett.*, vol. 25, no. 4, pp. 586–590, Apr. 2018.
- [17] A. Haqiqatnejad, F. Kayhan, and B. Ottersten, "Symbol-level precoding design based on distance preserving constructive interference regions," *IEEE Trans. Signal Process.*, vol. 66, no. 22, pp. 5817–5832, Nov. 2018.
- [18] A. Haqiqatnejad, F. Kayhan, and B. Ottersten, "An approximate solution for symbol-level multiuser precoding using support recovery," in *IEEE Workshop Signal Process. Adv. Wireless Commun. (SPAWC)*, Cannes, France, Jul. 2019, pp. 1–5.
- [19] K. L. Law and C. Masouros, "Symbol error rate minimization precoding for interference exploitation," *IEEE Trans. Commun.*, vol. 66, no. 11, pp. 5718–5731, Nov. 2018.
- [20] A. Salem and C. Masouros, "On the error probability of interference exploitation precoding with power allocation," in *IEEE Wireless Commun. Networking Conf. (WCNC)*, Seoul, Korea (South), May 2020, pp. 1–6.
- [21] M. Shao, Q. Li, and W.-K. Ma, "Minimum symbol-error probability symbol-level precoding with intelligent reflecting surface," *IEEE Wireless Commun. Lett.*, vol. 9, no. 10, pp. 1601–1605, Oct. 2020.
- [22] M. Alodeh, S. Chatzinotas, and B. Ottersten, "Constructive multiuser interference in symbol level precoding for the MISO downlink channel," *IEEE Trans. Signal Process.*, vol. 63, no. 9, pp. 2239–2252, May 2015.
- [23] K. L. Law and C. Masouros, "Constructive interference exploitation for downlink beamforming based on noise robustness and outage probability," in *IEEE Int. Conf. Acoust., Speech Signal Process. (ICASSP)*, Shanghai, China, Mar. 2016, pp. 3291–3295.
- [24] A. Haqiqatnejad, F. Kayhan, and B. Ottersten, "Symbol-level precoding design for max-min SINR in multiuser MISO broadcast channels," in *IEEE Workshop Signal Process. Adv. Wireless Commun. (SPAWC)*, Kalamata, Greece, June 2018, pp. 1–5.
- [25] L. Zhang, L. Gui, X. Mo, and X. Sang, "Symbol error rate minimization based constructive interference precoding for multi-user systems," *IEEE Access*, vol. 9, pp. 42 543–42 555, Mar. 2021.
- [26] F. Sohrabi, H. V. Cheng, and W. Yu, "Robust symbol-level precoding via autoencoder-based deep learning," in *IEEE Int. Conf. Acoust., Speech Signal Process. (ICASSP)*, Barcelona, Spain, May 2020, pp. 8951–8955.
- [27] J. Chen, A. Dholakia, E. Eleftheriou, M. Fossorier, and X.-Y. Hu, "Reduced-complexity decoding of LDPC codes," *IEEE Trans. Commun.*, vol. 53, no. 8, pp. 1288–1299, Aug. 2005.
- [28] J. Tan, Y. Xiao, C. Wu, and W. Tang, "Accurate log-likelihood ratio calculation for vector perturbation precoding," *IEEE Trans. Veh. Technol.*, vol. 70, no. 6, pp. 6272–6276, Jun. 2021.
- [29] K. Häggglund and E. Axell, "Adaptive demodulation in impulse noise channels," *IEEE Trans. Veh. Technol.*, vol. 71, no. 2, pp. 1685–1698, Feb. 2022.
- [30] K. Häggglund and E. Axell, "Adaptive demodulation in symmetric alpha-stable impulse noise channels," in *2020 IEEE Veh. Technol. Conf. (VTC)*, Antwerp, Belgium, May 2020, pp. 1–5.
- [31] S. Zheng, X. Zhou, S. Chen, P. Qi, C. Lou, and X. Yang, "Demodnet: Learning soft demodulation from hard information using convolutional neural network," in *2022 IEEE Int. Conf. Commun. (ICC)*, Seoul, Korea, Sept. 2022, pp. 1–6.
- [32] A. Li, F. Liu, X. Liao, Y. Shen, and C. Masouros, "Symbol-level precoding made practical for multi-level modulations via block-level rescaling," in *IEEE Workshop Signal Process. Adv. Wireless Commun. (SPAWC)*, Lucca, Italy, Sept. 2021, pp. 71–75.
- [33] D. J. Costello and G. D. Forney, "Channel coding: The road to channel capacity," *Proceedings of the IEEE*, vol. 95, no. 6, pp. 1150–1177, 2007.
- [34] K. Arora, J. Singh, and Y. S. Randhawa, "A survey on channel coding techniques for 5G wireless networks," *Telecommun. Syst.*, vol. 73, pp. 637–663, 2020.
- [35] R. Gallager, "Low-density parity-check codes," *IRE Trans. Inf. Theory*, vol. 8, no. 1, pp. 21–28, Jan. 1962.
- [36] P. Neshastegaran and A. H. Banihashemi, "Log-likelihood ratio calculation for pilot symbol assisted coded modulation schemes with residual phase noise," *IEEE Trans. Commun.*, vol. 67, no. 5, pp. 3782–3790, 2019.
- [37] J. Hagenauer, E. Offer, and L. Papke, "Iterative decoding of binary block and convolutional codes," *IEEE Trans. Inf. Theory*, vol. 42, no. 2, pp. 429–445, Mar. 1996.
- [38] Z. Hu, F. Chen, M. Wen, F. Ji, and H. Yu, "Low-complexity LLR calculation for OFDM with index modulation," *IEEE Wireless Commun. Lett.*, vol. 7, no. 4, pp. 618–621, 2018.
- [39] Y. Wang, W. Wang, L. You, C. G. Tsinos, and S. Jin, "Weighted MMSE precoding for constructive interference region," *IEEE Wireless Commun. Lett.*, vol. 11, no. 12, pp. 2605–2609, 2022.
- [40] Y. Wang, H. Hou, W. Wang, and X. Yi, "Symbol-level precoding for average SER minimization in multiuser MISO systems," submitted to *IEEE Wireless Commun. Lett.*, 2023. [Online]. Available: <https://arxiv.org/pdf/2310.07436.pdf>
- [41] D. A. Reynolds, "Gaussian mixture models," *Encyclopedia of biometrics*, vol. 741, no. 659–663, 2009.
- [42] S. M. Kay, *Fundamentals of statistical signal processing: estimation theory*. Prentice-Hall, Inc., 1993.
- [43] M. Zaheer, H. Kottur, and S. Ravanbakhsh, "Deep sets," in *Adv. neural inf. proces. syst.*, vol. 30, Dec. 2017.
- [44] J. Lee, Y. Lee, and J. Kim, "Set transformer: A framework for attention-based permutation-invariant neural networks," in *Proceedings of the 36th International Conference on Machine Learning*, ser. Proceedings of Machine Learning Research, vol. 97. PMLR, June 2019, pp. 3744–3753.
- [45] K. Pratik, B. D. Rao, and M. Welling, "Re-MIMO: Recurrent and permutation equivariant neural MIMO detection," *IEEE Trans. Signal Process.*, vol. 69, pp. 459–473, Dec. 2021.
- [46] A. Vaswani, N. Shazeer, and N. Parmar, "Attention is all you need," in *Adv. neural inf. proces. syst.*, vol. 30, 2017.
- [47] X.-D. Zhang, *Modern signal processing*. Walter de Gruyter GmbH & Co KG, 2022.
- [48] J. V. Candy, *Bayesian signal processing: classical, modern, and particle filtering methods*. John Wiley & Sons, 2016, vol. 54.
- [49] A. P. Dempster, N. M. Laird, and D. B. Rubin, "Maximum likelihood from incomplete data via the EM algorithm," *Journal of the Royal Statistical Society: Series B (Methodological)*, vol. 39, no. 1, pp. 1–22, 1977.
- [50] S. Balakrishnan, M. J. Wainwright, and B. Yu, "Statistical guarantees for the EM algorithm: From population to sample-based analysis," 2017.
- [51] S. ten Brink, "Convergence behavior of iteratively decoded parallel concatenated codes," *IEEE Trans. Commun.*, vol. 49, no. 10, pp. 1727–1737, Oct. 2001.
- [52] M. El-Hajjar and L. Hanzo, "EXIT charts for system design and analysis," *IEEE Commun. Surv. Tutor.*, vol. 16, no. 1, pp. 127–153, May 2013.